Closed-Form Absorbed-Power Dosimetry from 1 to 100 GHz

Robin Wydaeghe*, Luc Martens, *Member, IEEE*, Günter Vermeeren, *Member, IEEE*, Emmeric Tanghe, *Member, IEEE*, and Wout Joseph, *Senior Member, IEEE*

***Abstract*—Regulatory dosimetry on the human body relies on Finite-Difference Time-Domain (FDTD) simulations, which grow to trillions of cells at high mmWave frequencies. From 1 to 100 GHz, we replace these simulations with closed-form Fresnel surface laws for opaque biological tissue. Locally, Absorbed Power Density (APD) is Incident Power Density (IPD) multiplied by normal-incidence transmission, an ambient-occlusion factor, and the positive incidence cosine. For unpolarized skin at 28 GHz, pseudo-Brewster compensation keeps angular transmission within 5.6% of normal incidence up to $75°$. Integrating the local law over the visible nonconvex body surface yields a generalized Cauchy whole-body identity with one geometry scalar. A layered transmission term captures the sub-6 GHz whole-body dip. On a 10^4-triangle mesh under 10^2 incident paths, this turns the absorbed-power map into one differentiable matrix-vector multiply, evaluated in under 10 ms on a GPU. The closed form is validated in four ways: Mie theory on lossy spheres, full polarization-aware Fresnel calculations on the Thelonious phantom, Sim4Life FDTD, and dosimetry literature across 168 volunteers and 5 FDTD phantoms. In the high-frequency regime, the error is below 5%, within the reported uncertainty in human-skin dielectric parameters. Whole-body compliance reduces to three precomputed scalars. Antenna and beam optimization under exposure constraints become differentiable end-to-end.**

***Index Terms*—APD, dosimetry, FDTD, Fresnel transmission, ICNIRP, mmWave, SAR.**

I. Introduction

Wireless exposure on the human body is regulated through two basic restrictions in the International Commission on Non-Ionizing Radiation Protection (ICNIRP) 2020 guidelines [1], IEC/IEEE 63195, and IEEE C95.1: the mass-averaged Specific Absorption Rate (SAR) below 6 GHz, with peak values evaluated as peak-spatial SAR averaged over a 10 g cube ($\text{psSAR}_{10\text{g}}$), and the surface-averaged absorbed power density (Absorbed Power Density (APD)) above 6 GHz. Direct evaluation uses Finite-Difference Time-Domain (FDTD) simulations on an anatomical phantom [2]–[5]. Resolving the submillimeter absorption layer at ten cells per in-tissue wavelength sets a cell count of 10^8 at 6 GHz, growing to 10^{12} near 100 GHz. A simulation campaign that covers frequencies, postures, and incidence directions takes weeks on Graphics Processing Unit (GPU) clusters. Whole-body simulations above 30 GHz become computationally difficult [5]. This work shows that the surface absorbed-power map on a 10^4-triangle body mesh reduces to one matrix-vector multiply, evaluated in under 10 ms on a commercial modern GPU at any frequency from 1 to 100 GHz. The whole-body absorbed power reduces to only three precomputed scalars: the body mass, the body surface area, and the flux-weighted Fresnel transmission.

Several groups already capture this absorption with a single fitted coefficient [2], [3], [6]–[9]. The coefficient is defined in different ways, as an efficiency, a normalized cross-section, or a transmission, but in every study it falls between about 0.4 and 0.7 above 6 GHz. This shared range points to a single underlying closed-form quantity. Each coefficient is fitted separately for each phantom and frequency from an FDTD sweep or a chamber measurement, so the values are slow to obtain, they differ between studies, and they provide no gradients for design. No study writes them as one expression, and none treats a nonconvex body in closed form.

This work derives the closed form behind these coefficients. On high-index tissue, the unpolarized Fresnel transmission collapses to a near-constant scalar [10]. The local law then integrates over a nonconvex body through a generalized Cauchy formula [11], with self-shadowing from ambient occlusion [12]–[14]. A layered correction in the fat layer covers the 3 GHz dip [7]. The five fitted coefficients are special cases of this expression. In the mmWave band it reproduces FDTD to within the tissue dielectric uncertainty, at a small fraction of the cost. Because it is also differentiable, antenna and beam design under exposure limits becomes a continuous optimization.

To the best of the authors' knowledge, this paper makes the following contributions.

1) We derive closed-form APD laws from Fresnel transmission on lossy biological tissue and integrate them over nonconvex anatomical meshes with a generalized Cauchy formula. Whole-body absorbed power reduces to a flux-weighted transmission scalar and an ambient-occlusion geometry scalar.
2) Pseudo-Brewster compensation simplifies the law further for unpolarized incidence. Transverse Electric (TE)/Transverse Magnetic (TM) cancellation keeps the geometric approximation within a few percent over the relevant angular range.

All authors are with the WAVES research group, Department of Information Technology, Ghent University–imec, Technologiepark-Zwijnaarde 126, 9052 Ghent, Belgium.

*Corresponding author. E-mail: robin.wydaeghe@ugent.be.

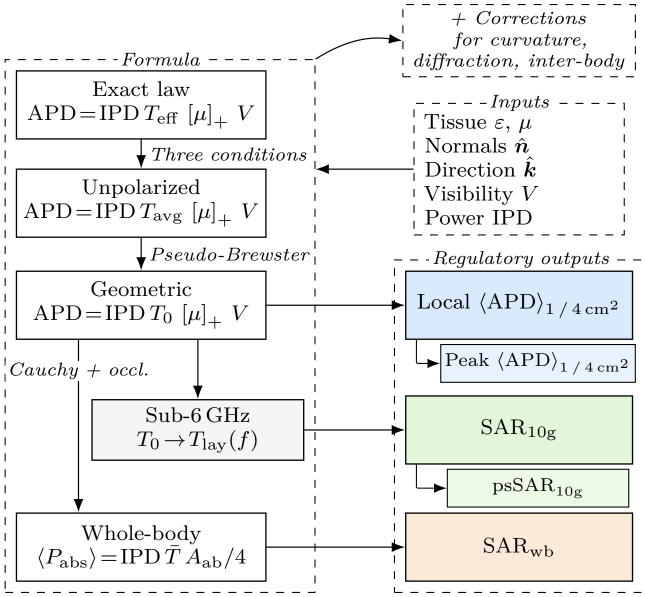

Fig. 1: Flowchart of our approach. The formula has five inputs. Three reductions take the exact law to a whole-body identity. Each arrow is one reduction, justified in Sections II-D, III and IV-B. A sub-6 GHz branch replaces T_0 with a layered transmission $T_{\text{lay}}(f)$ (Section IV-C). Higher-order corrections are bounded errors on the chain (Section V-F). The chain has three regulatory outputs: surface-averaged absorbed power density $\langle\text{APD}\rangle_{1\,/\,4\,\text{cm}^2}$, peak-spatial SAR in a 10 g cube $\text{psSAR}_{10\text{g}}$, and whole-body SAR SAR_{wb}. Smaller boxes are the peak-spatial versions used by ICNIRP (Section VI).

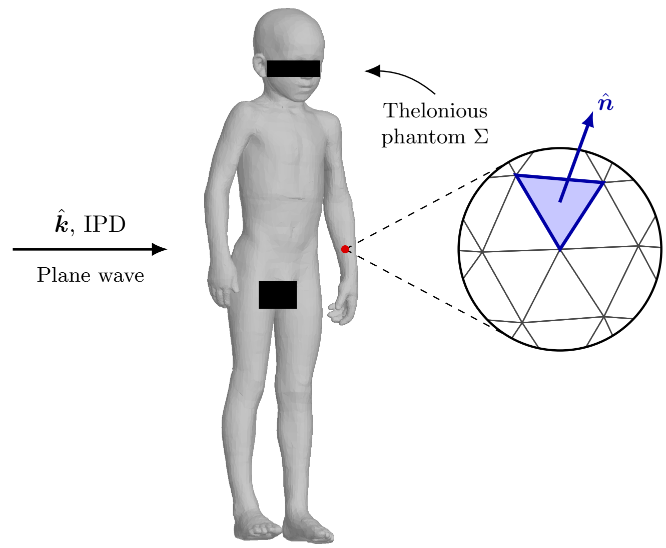

Fig. 2: Configuration of the dosimetry problem. A plane wave with intensity IPD and direction $\hat{\boldsymbol{k}}$ illuminates the Thelonious phantom. The local APD at a visible surface point is APD $=$ IPD $T(\theta)\cos\theta$, with θ the angle between $-\hat{\boldsymbol{k}}$ and the outward normal $\hat{\boldsymbol{n}}$ on the triangulated body surface, and T the Fresnel transmission.

3) The computation is differentiable end-to-end. For a body mesh under many incident paths, the absorbed-power map is one 10 ms matrix-vector multiply.
4) Higher-order correction terms extend and delimit the closed form. A layered transmission term covers the sub-6 GHz whole-body comparison, while curvature, diffraction, and inter-body reflection terms bound the main higher-order errors.
5) The theory is validated in four independent ways: Mie theory on lossy spheres, full polarization-aware Fresnel calculations on the Thelonious phantom, Sim4Life FDTD, and dosimetry literature across 168 volunteers and 5 FDTD phantoms.

II. Method: Local Absorption Law

Flowchart 1 shows the exact local law, the reductions to whole-body absorbed power, the higher-order corrections, and the regulatory outputs. This section derives the top box: the local law at one visible surface point.

A. Configuration

Figure 2 shows the considered configuration. A plane wave with intensity IPD and direction $\hat{\boldsymbol{k}}$ illuminates the body, and we evaluate APD($\mathbf{r}$) at each visible surface point.

A harmonic plane wave with time-averaged Poynting vector $\mathbf{S}_{\text{inc}} = \text{IPD}\,\hat{\boldsymbol{k}}$ (units W/m^2) illuminates a body. Three working assumptions hold throughout. First, the surface Σ is locally flat on the wavelength scale. Second, the skin depth at every frequency of interest is much smaller than any body dimension, so all power transmitted through the surface is absorbed within a thin surface layer. Third, coherent reflections from internal tissue interfaces and from other body parts are neglected at this stage and re-enter as bounded corrections in Sections IV and V-F. At a surface point $\mathbf{r}$ with outward unit normal $\hat{\boldsymbol{n}}(\mathbf{r})$, the incidence cosine is $\mu(\mathbf{r}) \equiv \hat{\boldsymbol{n}}(\mathbf{r}) \cdot (-\hat{\boldsymbol{k}}) = \cos\theta_i(\mathbf{r})$. A front-facing point has $\mu > 0$; a point facing away from the source has $\mu \le 0$.

B. Power flux through the surface

The inward power flux through a surface element $\mathrm{d}A$ at $\mathbf{r}$ is $\mathrm{d}P_{\text{in}} = \text{IPD}\,\mu\,\mathrm{d}A$. The reflected wave propagates in the specular direction with power density $|r(\theta_i)|^2\,\text{IPD}$, where $r(\theta_i)$ is the Fresnel amplitude reflection coefficient appropriate to the polarization. Energy conservation at a lossy half-space gives

$$\text{APD}(\mathbf{r}) = \text{IPD} \cdot T(\theta_i) \cdot \mu(\mathbf{r}), \qquad T(\theta_i) \equiv 1 - |r(\theta_i)|^2\,, \quad (1)$$

for each polarization separately.

C. Fresnel coefficients

The body surface is modeled as a planar interface between free space ($n_1 = 1$) and a lossy medium with complex refractive index $\tilde{n} = \sqrt{\varepsilon_r - i\sigma/(\omega\varepsilon_0)}$. The normal component of the wave vector inside the medium is $\xi = \sqrt{\tilde{n}^2 - 1 + \mu^2}$ with $\text{Re}(\xi) > 0$. Continuity of the tangential fields gives

$$r_s = \frac{\mu - \xi}{\mu + \xi}, \qquad r_p = \frac{\tilde{n}^2\,\mu - \xi}{\tilde{n}^2\,\mu + \xi}\,, \quad (2)$$

for TE and TM polarizations, respectively. The corresponding power-absorption coefficients are $T_s(\theta) = 1 - |r_s|^2$ and $T_p(\theta) = 1 - |r_p|^2$. At normal incidence, $\mu = 1$ and $\xi = \tilde{n}$, giving the polarization-degenerate value

$$T_0 \equiv T_s(0) = T_p(0) = \frac{4\,\mathrm{Re}(\tilde{n})}{|1+\tilde{n}|^2}\,. \tag{3}$$

For skin at 28 GHz with $\varepsilon_r = 16.55$ and $\sigma = 25.8$ S/m, $\tilde{n} = 4.49 - 1.79i$ and $T_0 = 0.539$.

D. Polarization-aware exact law

A plane wave is fully polarized. At a surface point $\mathbf{r}$, decompose the incident electric field into local TE and TM components by projecting on the unit vectors $\hat{e}_s(\mathbf{r}) = \hat{\boldsymbol{k}}\times\hat{\boldsymbol{n}}/|\hat{\boldsymbol{k}}\times\hat{\boldsymbol{n}}|$ and $\hat{e}_p(\mathbf{r}) = \hat{e}_s\times\hat{\boldsymbol{k}}$. Let $\mathbf{E}_0 = a_s\hat{e}_s + a_p\hat{e}_p$, with the local TE and TM energy fractions $|e_s|^2 = |a_s|^2/|\mathbf{E}_0|^2$ and $|e_p|^2 = |a_p|^2/|\mathbf{E}_0|^2$. The effective transmission at $\mathbf{r}$ is then

$$T_{\mathrm{eff}}(\mathbf{r}) = |e_s(\mathbf{r})|^2\,T_s(\theta) + |e_p(\mathbf{r})|^2\,T_p(\theta)\,. \tag{4}$$

The exact APD at a visible point is therefore

$$\mathrm{APD}(\mathbf{r}) = \mathrm{IPD}\,T_{\mathrm{eff}}(\mathbf{r})\;[\mu(\mathbf{r})]_+\,. \tag{5}$$

Equation (5) holds for any polarization, any frequency where the body is opaque, and any locally flat surface. The self-shadowing factor $V(\mathbf{r},\hat{\boldsymbol{k}})$ of the geometric law in Section III is suppressed in this subsection because the Fresnel calculation operates at a point already taken to be visible. Visibility re-enters with the multi-source matrix form in Section III-F.

To proceed, write

$$T_{\mathrm{eff}}(\mathbf{r}) = T_{\mathrm{avg}}(\theta) + \tfrac{1}{2}\,q(\mathbf{r})\,\Delta T(\theta)\,, \tag{6}$$

with $T_{\mathrm{avg}} = \frac{1}{2}(T_s + T_p)$ the unpolarized baseline, $\Delta T = T_p - T_s$ the polarization splitting, and $q = |e_p|^2 - |e_s|^2 \in [-1, 1]$ the local TM excess. The polarization correction vanishes pointwise for circular illumination, in expectation for random-orientation linear illumination, and to within 2.5% for multipath averaging above 20 paths. First, for circular polarization the TE and TM intensities are equal at every point on every body, so $q \equiv 0$ pointwise. Second, for linear polarization with random ensemble orientation either in space or time, the ensemble average $\langle q\rangle$ vanishes by the same argument. Third, for a body in a multipath environment with N independent path orientations, the variance of the polarization correction scales as $D_B/\sqrt{2N}$, where $D_B \le 16\%$ is the body's polarization directivity on the Thelonious phantom, and for $N \ge 20$ paths the correction drops below 2.5%. Section **??** of the SI derives all three conditions and the $D_B/\sqrt{2N}$ variance bound. Under any of these conditions the exact law reduces to

$$\mathrm{APD}(\mathbf{r}) = \mathrm{IPD}\,T_{\mathrm{avg}}(\theta(\mathbf{r}))\;[\mu(\mathbf{r})]_+\,. \tag{7}$$

The angular dependence is now confined to the scalar function $T_{\mathrm{avg}}(\theta)$. The next section shows that this function is nearly constant for biological tissue.

TABLE I: Fresnel transmission for skin at 28 GHz. Here $T_0 = T_{\mathrm{avg}}(0)$ is the normal-incidence value, and T_{avg}/T_0 stays within 5.6% of unity over $[0°, 75°]$.

θ	T_s (TE)	T_p (TM)	T_{avg}	T_{avg}/T_0
0°	0.539	0.539	0.539	1.000
30°	0.489	0.591	0.540	1.002
45°	0.422	0.666	0.544	1.010
60°	0.321	0.791	0.556	1.032
70°	0.233	0.902	0.568	1.054
75°	0.182	0.952	0.567	1.053

III. Method: pseudo-Brewster compensation

The flowchart now moves from the exact local law to its unpolarized form. This section shows why the Fresnel factor can be replaced by a nearly constant scalar for mmWave tissue. The reason is pseudo-Brewster compensation.

A. Mechanism

The Brewster angle of a lossless dielectric is $\theta_{\mathrm{B}} = \arctan(n_2/n_1)$, at which the TM reflection coefficient vanishes [15]. For a lossy dielectric the reflection minimum is finite but small. The angle at which $|r_p|^2$ is minimized is the *pseudo-Brewster angle* and satisfies $\theta_{\mathrm{pB}} \approx \arctan|\tilde{n}|$ to within 1° for $|\tilde{n}| > 3$ [16], [17]. At this angle, T_p peaks near 0.95, while T_s has fallen below 0.20. Their average $T_{\mathrm{avg}}(\theta_{\mathrm{pB}}) \approx 0.5$ is close to the normal-incidence value $T_0 \approx 0.5$–0.6 for biological tissue at mmWave.

Azzam [10] showed that for lossless dielectric substrates with refractive index $|\tilde{n}| > 2 + \sqrt{3} \approx 3.73$, the unpolarized reflectance varies by less than 1% over $[0°, 60°]$. Empirically, the near-constancy extends to $|\tilde{n}| > 2.5$, below the strict Azzam threshold. The SI evaluates this extension on the IT'IS tissue-properties database [18], [19]. Biological tissue at the wireless mmWave band has $|\tilde{n}| \in [3, 6]$, putting it in the high-index regime. This connection between the Azzam criterion and biological dosimetry has not appeared in the optics or bioelectromagnetics literature, where prior work has evaluated the angular and polarization dependence of body transmission above 6 GHz numerically [20] without the high-index reduction.

B. Quantitative behavior across angle

Figure 3 illustrates the compensation for skin at 28 GHz. Figure 3a shows T_s, T_p, and T_{avg} versus incidence angle. Figure 3b shows the APD $\mathrm{APD}/\mathrm{IPD} = T(\theta)\cos\theta$ for each polarization and for the simplified product $T_0\cos\theta$. The unpolarized curve closely tracks the simplified prediction, and the small gap is the Fresnel approximation error.

Table I quantifies the deviation of T_{avg} from T_0 across $[0°, 75°]$ on skin at 28 GHz. The maximum deviation is 5.6% at 70–75°. Below 30° the agreement is at the fourth significant figure.

C. Tissue universality

All biological tissues at the wireless mmWave band cluster in the $|\tilde{n}| > 2.5$ region where the compensation

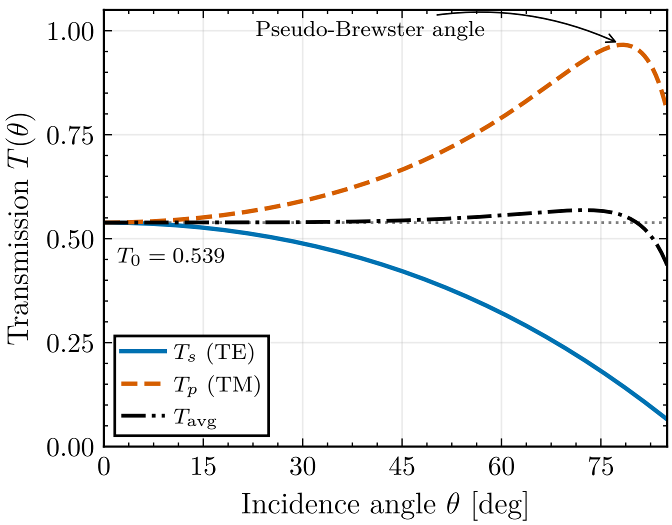

(a) Fresnel transmission T.

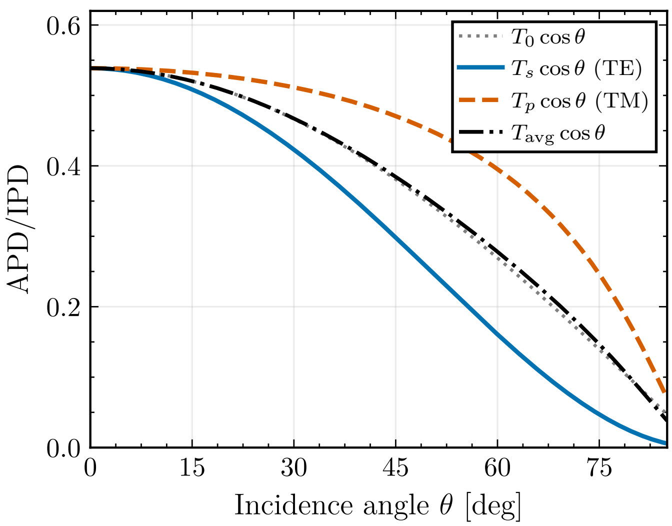

(b) Normalized absorbed power APD/IPD.

Fig. 3: Pseudo-Brewster compensation for skin at 28 GHz ($\tilde{n} = 4.49 - 1.79i$, $T_0 = 0.539$). (a) Fresnel power-absorption coefficients T_s (TE), T_p (TM), and $T_{avg} = \frac{1}{2}(T_s + T_p)$ versus incidence angle θ. T_{avg} stays within 5.6% of T_0 up to 75°. (b) Normalized absorbed power APD/IPD $= T(\theta)\cos\theta$ for the same three states. The dotted reference is the simplified $T_0 \cos\theta$ prediction.

operates. Table II lists the relevant parameters at 28 GHz from the IT'IS tissue-properties database [18], [19]. Skin and muscle have $|\tilde{n}|$ near 5 and an angular variation below 5.6%. Water has $|\tilde{n}| > 6$ and a variation below 4%. Fat is the outlier, with $|\tilde{n}| \approx 2$ and an 8.2% variation, but fat is rarely the outermost tissue at exposure sites of regulatory interest. Above 6 GHz, the relevant outermost tissues are skin, subcutaneous fat, and vitreous humor.

TABLE II: Pseudo-Brewster compensation across tissue types at 28 GHz. The variation column is the maximum deviation of T_{avg}/T_0 from unity over $[0°, 75°]$.

Tissue	ε_r	σ [S/m]	$\lvert\tilde{n}\rvert$	T_0	T_{avg} var.
Skin	17.0	25.0	4.84	0.54	5.6%
Muscle	25.0	30.0	5.62	0.48	4.8%
Fat	4.0	2.0	2.05	0.77	8.2%
Water	25.0	55.0	6.62	0.45	3.9%

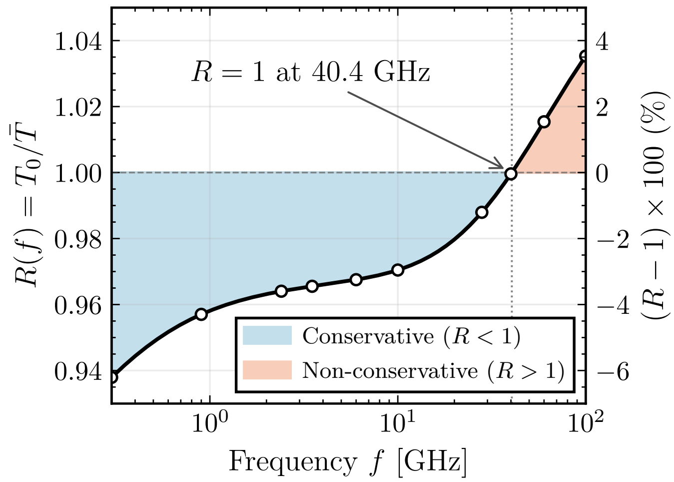

Fig. 4: Sphere ratio $R(f) = T_0/\bar{T}$ versus frequency for skin (IT'IS tissue-properties database [18], [19]). $R = 1$ indicates that the constant-T_0 approximation is exact on the direction-averaged quantity; $R < 1$ means T_0 underestimates absorbed power and $R > 1$ means it overestimates. The dashed horizontal lines mark the ±4% band.

D. Frequency dependence

The accuracy of the constant-T_0 approximation has a clean frequency dependence. Define the sphere ratio $R(f)$

$$R(f) \equiv T_0(f)/\bar{T}(f), \qquad \bar{T}(f) \equiv 2\int_0^1 T_{avg}(\mu, f)\,\mu\,\mathrm{d}\mu\,, \tag{8}$$

where $\bar{T}(f)$ is the flux-weighted Fresnel transmission. $R(f) = 1$ when the constant-T_0 approximation is exact on a direction-averaged quantity. $R < 1$ means T_0 underestimates absorbed power. $R > 1$ means it overestimates. Figure 4 shows that for skin the crossover is at 40.4 GHz, where the compensation is exact. Below this frequency the approximation underestimates absorbed power. Above, it overestimates by at most 3.5% at 100 GHz. The root-mean-square error remains below 5% across 0.3–100 GHz. Frequency-resolved Cole–Cole values for skin and the angle family $T_{avg}(\theta)\cos\theta$ at six representative frequencies are in Table **??** and Fig. **??** of the SI.

E. Geometric absorption law

Two simplifications act on the exact law in (5). First, we apply the polarization reduction (7). Second, we substitute $T_{avg}(\theta) \to T_0$ and reinstate self-shadowing through the binary visibility $V(\mathbf{r},\hat{\boldsymbol{k}})\in\{0,1\}$. The exact law reduces to the *geometric absorption law*

$$\boxed{\mathrm{APD}(\mathbf{r})\approx\mathrm{IPD}\cdot T_0\cdot V(\mathbf{r},\hat{\boldsymbol{k}})\cdot\Big[\hat{\boldsymbol{n}}(\mathbf{r})\cdot(-\hat{\boldsymbol{k}})\Big]_+}\,. \tag{9}$$

The tissue physics enters through the scalar T_0. All spatial variation depends on the body shape through the surface-normal field $\hat{\boldsymbol{n}}(\mathbf{r})$ and the visibility field $V(\mathbf{r},\hat{\boldsymbol{k}})$. For a convex body $V\equiv 1$ and (9) reduces to the classical convex form $\mathrm{IPD}\,T_0\Big[\hat{\boldsymbol{n}}\cdot(-\hat{\boldsymbol{k}})\Big]_+$. Figure 5 shows how visibility enters the geometric law on the Thelonious phantom. Panel (a) shows the frontal APD map. Panels (b) and (c) show the direction-isotropic exposure fraction $\eta(\mathbf{r})$ from the front and side. Under frontal illumination the medial thighs, the inside of the wrists, and the underside of the chin become self-shadowed and drop to zero through V. The transmission coefficient T_{tr} fitted in [2], [3], [21] is identified with T_0, the normal-incidence transmission.

Hence, the error of (9) relative to the exact polarization-aware law is bounded by the maximum of the polarization correction and the angular variation of T_{avg}. The latter is below 5% across the wireless mmWave band (6–100 GHz). The former is below 2.5% for $N\geq 20$ independent multipath components, and at most 16% on a real human body for the worst-case linearly polarized single plane wave. The combined error is below the 20% uncertainty in tissue dielectric properties at mmWave [22].

F. Discrete multi-source form

Equation (9) extends to a triangle mesh under multiple incident waves. Discretize the body into M triangles. Row j of $\mathbf{N}\in\mathbb{R}^{M\times 3}$ holds the outward unit normal $\hat{\boldsymbol{n}}_j$. Let N plane waves arrive with unit directions $\hat{\boldsymbol{k}}_1,\ldots,\hat{\boldsymbol{k}}_N$ and power densities $S_1,\ldots,S_N$. Stack the directions column-wise into $\mathbf{K}\in\mathbb{R}^{3\times N}$, with column i equal to $-\hat{\boldsymbol{k}}_i$. Stack the powers into $\mathbf{s}=[S_1,\ldots,S_N]^\top\in\mathbb{R}^N$. Let $\mathbf{V}\in\{0,1\}^{M\times N}$ be the visibility matrix, with $V_{ji}=1$ when direction $\hat{\boldsymbol{k}}_i$ reaches triangle j, and $V_{ji}=0$ otherwise. Collect the per-triangle APD values into $\mathbf{APD}\in\mathbb{R}^M$.

The geometric law on the mesh then reads

$$\mathbf{APD}=T_0\left([\mathbf{N}\,\mathbf{K}]_+\odot\mathbf{V}\right)\mathbf{s}\,. \tag{10}$$

The cosine matrix $\mathbf{N}\,\mathbf{K}\in\mathbb{R}^{M\times N}$ has entry (j,i) equal to $\hat{\boldsymbol{n}}_j\cdot(-\hat{\boldsymbol{k}}_i)$. The operator $[\cdot]_+\equiv\max(\cdot,0)$ acts component-wise, and clamps back-facing entries to zero. The Hadamard product $\odot$ with $\mathbf{V}$ gates self-shadowed entries. The product with $\mathbf{s}$ sums the contributions of the N incident waves.

Each step is differentiable. The operator $[\cdot]_+$ is the rectified linear unit (ReLU). Replacing it with the smooth Gaussian Error Linear Unit (GELU) activation [23] leaves the structure intact and replaces the hard cutoff with a soft rolloff (Eq. (16)). Gradients of regulatory quantities with respect to antenna positions, antenna orientations, and RIS phases propagate through any differentiable ray tracer [24]. The arithmetic primitive is the per-pixel shading operation that consumer GPUs run at sub-millisecond rates, with the cosine gate as rectified shading and $\mathbf{V}$ as ambient occlusion. For $M\approx 10^4$ and $N\approx 10^2$, the spatial map is one matrix-vector multiply on the GPU.

IV. Method: whole-body absorbed power

The flowchart next integrates the geometric local law over the body. This section turns surface APD into direction-averaged whole-body absorbed power. The needed new ingredient is visibility: nonconvex body parts can shadow one another.

A. Self-shadowing and ambient occlusion

The human body is not convex. Concavities such as the armpits, the gap between the legs, and the neck region cause one part of the body to shadow another. The binary visibility $V(\mathbf{r},\hat{\boldsymbol{k}})\in\{0,1\}$ in (9) is the ambient-occlusion primitive of computer graphics introduced by Zhukov *et al.* [12] and brought into production rendering by Landis [13]. Modern GPUs evaluate $V(\mathbf{r},\hat{\boldsymbol{k}})$ at interactive frame rates [14].

The *exposure fraction* η at a surface point $\mathbf{r}$ is the cosine-weighted fraction of the upper hemisphere from which $\mathbf{r}$ is unobstructed,

$$\eta(\mathbf{r})=\frac{1}{\pi}\int_{S^2}\Big[\hat{\boldsymbol{n}}(\mathbf{r})\cdot(-\hat{\boldsymbol{k}})\Big]_+V(\mathbf{r},\hat{\boldsymbol{k}})\,\mathrm{d}\Omega\,. \tag{11}$$

For convex bodies $V\equiv 1$ and $\eta\equiv 1$. For nonconvex bodies $\eta\in[0,1]$.

The exposure fraction η is mathematically identical to the self-shadowing factor γ_s that Flintoft *et al.* define as "the proportion of total surface area of the body that is illuminated by the reverberant field" [7, p. 3301] and estimate geometrically as 0.75–0.85 from Tomita's surface-area data [25]. The Flintoft estimate is geometric and posture-dependent. The construction here is computational and posture-resolved. For the Thelonious phantom, an ambient-occlusion solver returns the area-weighted mean $\bar{\eta}=A_{\mathrm{ab}}/A=0.865$. This is near the upper end of Flintoft's band $[0.75,0.85]$ [25], and is rendered on the phantom in Fig. 5b and Fig. 5c. Most of the body has $\eta\approx 1$. Reductions occur in concavities. The medial sides of the legs and arms, the armpits, the underside of the chin, and the soles of the feet are the dominant such regions. On a 10^4–10^5 triangle mesh the solver evaluates η in tens of milliseconds on commodity hardware.

B. Generalized Cauchy formula

The generalized Cauchy formula is the central whole-body identity.

Theorem 1. *Let a body Σ have surface area A, exposure fraction $\eta(\mathbf{r})$, and absorption area $A_{\mathrm{ab}}\equiv\int_\Sigma\eta(\mathbf{r})\,\mathrm{d}A$. Under isotropic, unpolarized plane-wave illumination of intensity* IPD *on tissue with normal-incidence transmission T_0, the direction-averaged whole-body absorbed power is*

$$\langle P_{\mathrm{abs}}\rangle=\mathrm{IPD}\,T_0\,A_{\mathrm{ab}}/4\,. \tag{12}$$

Proof. Apply Fubini's theorem to exchange the surface and direction integrals. The local law (9) gives $\mathrm{APD}(\mathbf{r},\hat{\boldsymbol{k}})=$

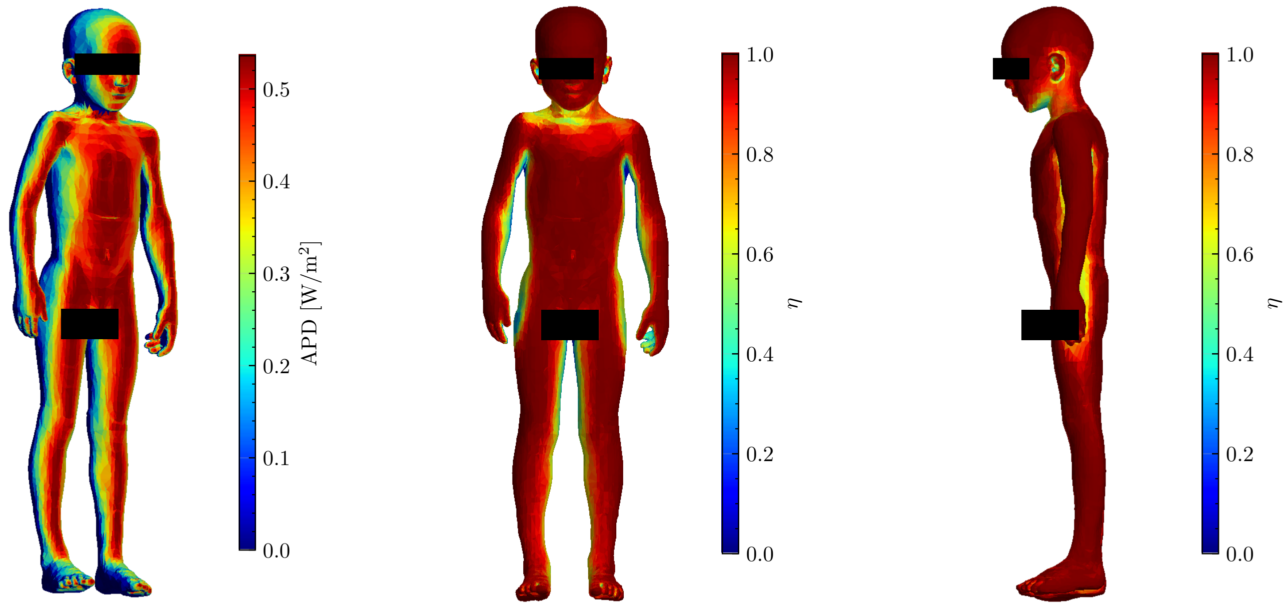

(a) APD($\mathbf{r}$), frontal $\hat{\boldsymbol{k}}$. (b) $\eta(\mathbf{r})$, front view. (c) $\eta(\mathbf{r})$, side view.

Fig. 5: APD and η maps on the Thelonious phantom (skin at 28 GHz, IPD = 1 W/m^2, area-weighted mean $\bar{\eta} = 0.865$). (a) APD under frontal illumination $\hat{\boldsymbol{k}} = +\hat{y}$. Front-facing triangles absorb at the cosine rate $T_0\,\mathrm{IPD}\cos\theta$. Self-shadowed elements drop to zero through $V(\mathbf{r}, \hat{\boldsymbol{k}})$. (b, c) Direction-isotropic exposure fraction $\eta(\mathbf{r}) \in [0, 1]$ from (11), front and side views. Panel (a) is the integrand of the Cauchy formula along one direction. Panels (b, c) integrate over the full sphere.

$\mathrm{IPD}\,T_0\,V(\mathbf{r}, \hat{\boldsymbol{k}})\,\left[\hat{\boldsymbol{n}} \cdot (-\hat{\boldsymbol{k}})\right]_+$. The direction average of the integrand is

$$\frac{1}{4\pi}\int_{S^2} \mathrm{IPD}\,T_0\,V(\mathbf{r}, \hat{\boldsymbol{k}})\,\left[\hat{\boldsymbol{n}} \cdot (-\hat{\boldsymbol{k}})\right]_+ \mathrm{d}\Omega = \frac{\mathrm{IPD}\,T_0}{4}\,\eta(\mathbf{r}),$$

using the definition of η and the identity $\int_{S^2}\left[\hat{\boldsymbol{n}} \cdot (-\hat{\boldsymbol{k}})\right]_+ \mathrm{d}\Omega = \pi$ for any unit $\hat{\boldsymbol{n}}$. Integration over Σ gives (12). □

The classical Cauchy formula $\langle A_\perp \rangle = A/4$ is the special case $\eta \equiv 1$, valid for any convex body. The absorption area A_{ab} reduces all geometric complexity of self-shadowing to a single scalar.

Let A_{CH} be the surface area of the convex hull of the body. Energy conservation under isotropic illumination implies $\langle P_{\mathrm{abs}} \rangle \leq \mathrm{IPD}\,A_{\mathrm{CH}}/4$, because the power entering the convex hull bounds the absorbed power. For the Thelonious phantom $A_{\mathrm{CH}}/A \approx 1.20$, so the hull bound brackets the true absorbed power within a few percent.

The constant-T_0 approximation in (12) is accurate to 5% root-mean-square across 0.3–100 GHz, but it is not exact. Replacing T_0 with the flux-weighted transmission $\bar{T}(f)$ defined in (8) removes the approximation.

The same direction-averaged identity becomes exact when T_0 is replaced by the angle-dependent $T_{\mathrm{avg}}(\theta)$. The cosine-weighted angular integral collapses to $\bar{T}$ via (8), so for any body opaque at the wavelength

$$\langle P_{\mathrm{abs}} \rangle = \mathrm{IPD}\,\bar{T}(f)\,A_{\mathrm{ab}}/4\,. \tag{13}$$

Equation (13) requires only electromagnetic opacity, a condition met above approximately 1 GHz on a torso and above approximately 6 GHz on a finger. Table III lists T_0, $\bar{T}$, and the ratio $R = T_0/\bar{T}$ for skin from 0.3–100 GHz.

TABLE III: Normal-incidence transmission T_0, flux-weighted transmission $\bar{T}$, and their ratio $R = T_0/\bar{T}$ for skin (IT'IS tissue-properties database [18], [19]).

f [GHz]	$\lvert\tilde{n}\rvert$	T_0	$\bar{T}$	R
0.3	7.93	0.381	0.406	0.938
0.9	6.70	0.445	0.465	0.957
2.4	6.29	0.470	0.488	0.964
6.0	6.07	0.481	0.497	0.968
10	5.87	0.489	0.504	0.971
28	4.84	0.536	0.543	0.988
40	4.30	0.570	0.571	1.000
60	3.68	0.622	0.613	1.015
100	3.01	0.701	0.677	1.035

The reverberation-chamber literature has been measuring $\bar{T}$ directly. Bamba's empirical efficiency $\eta(f)$ for diffuse-field exposure on four FDTD ellipsoid phantoms [6] coincides with $\bar{T}(f)$ to 3% at 5.8 GHz. It diverges below 3 GHz, where the body-Mie contribution to absorption on a finite ellipsoid becomes non-negligible (Table VIII). The framework is mainly a mmWave method. Flintoft's plateau $\langle Q^a \rangle/\gamma_s = 0.47$–$0.49$ at 7–11 GHz matches $\bar{T}$ at the same frequencies to 2% [7]. Zhang's plateau $\xi = 0.45$–0.65 above 6 GHz brackets $\bar{T} \cdot A_{\mathrm{ab}}/A$ [8].

C. Layered transmission below 6 GHz

Above 6 GHz, (13) matches the plateau values reported by Bamba, Flintoft, and Zhang. Below 6 GHz, Flintoft and Zhang observe a structured dip near 3 GHz that the homogeneous half-space model does not reproduce [7], [8]. The dip is anatomical. Flintoft's negative correlation of $\langle Q^a \rangle$ with mean subcutaneous fat thickness d_{SF} is steepest at 3 GHz ($-0.0061\,\mathrm{mm}^{-1}$, $R^2 = 0.40$, [7, Table 6]), with the slope falling to $-0.0030\,\mathrm{mm}^{-1}$ at 7–11 GHz.

The mechanism is a Fabry–Pérot resonance in the subcutaneous fat layer. Below 6 GHz the SAR penetration depth in fat exceeds 70 mm, against fat thicknesses of 2–20 mm in the Flintoft cohort [7, Table 1]. The wave passes through the fat layer with little attenuation and reflects from the fat-muscle interface. Constructive interference enhances absorption, and destructive interference suppresses it. A three-layer transfer-matrix model with skin, fat, and a semi-infinite muscle half-space gives the layered transmission

$$T_{\mathrm{lay}}(f, d_{\mathrm{SF}}) = 1 - \left|\widetilde{\Gamma}_1(f, d_{\mathrm{SF}})\right|^2, \tag{14}$$

where $\widetilde{\Gamma}_1$ is the generalized Fresnel reflection coefficient at the air-skin interface, computed recursively from the fat-muscle interface upward [15], [26]. Section **??** of the SI gives the full Chew recursion, the standing-wave SAR per layer, and the layer-by-layer cube integral. Fig. **??** of the SI shows $T_{\mathrm{lay}}(f)$ for the canonical 2 mm skin / 10 mm fat / muscle stack. Replacing $\bar{T}$ with T_{lay} in (13) gives a frequency-dependent direction-averaged absorbed power that includes the fat-layer resonance. For a fat thickness of 10 mm the model predicts a 40% enhancement above the homogeneous prediction at 0.9 GHz (quarter-wave matching) and a 27% reduction at 3.5 GHz (destructive interference).

Zhang derives the planar limit of this model in his thesis [8, Sec. 2.2] and observes the resonance shift with fat thickness in his Figs. 2.7–2.8, writing that "the fat layer may act as a matching layer between skin and muscle" [8, p. 21]. The contribution here is to embed the planar model in the body-surface integral via T_{lay} and (13), which makes the resonance compatible with a Cauchy-style direction average. Body-surface averaging suppresses the oscillation by a factor of approximately $A_{\mathrm{exposed,fat}}/A$ because different body regions carry different fat thicknesses, with limbs near 2 mm and abdomen near 30 mm, and consequently different resonance frequencies. The integrated dip is shallower than the single-thickness prediction but is at the same frequency. The local surface map $\mathrm{APD}(\mathbf{r}) \approx \mathrm{IPD}\, T_0 V\, [\mu]_+$ loses pointwise meaning below 6 GHz, where the SAR penetration depth exceeds the surface layer thickness. Total power remains valid via T_{lay} throughout.

V. Validation and error analysis

We validate the theory four ways: (i) Mie theory on lossy spheres, (ii) full polarization-aware Fresnel calculations on the Thelonious phantom, (iii) Sim4Life FDTD on the same phantom, and (iv) the reverberation-chamber and FDTD literature across 168 volunteers and 5 phantoms. The four checks isolate, respectively, the Fresnel approximation, realistic anatomy, volumetric FDTD agreement, and population-level scaling. We then add the higher-order corrections for curvature, diffraction, and inter-body reflection, and close with a single error budget that propagates the dielectric uncertainty.

A. Configuration

Thelonious is a 6-year-old male phantom from the Virtual Population [18], shown in Fig. 5. The surface is a high-resolution triangle mesh with 23,826 faces. Tissue properties at every frequency follow the tissue-properties database [18], [19]. Mie benchmarks use lossy spheres of skin permittivity at the listed frequencies, evaluated with the standard recursive series of Bohren and Huffman [27]. Sim4Life FDTD runs use the 0.45–5.8 GHz band on the same Thelonious mesh embedded in a free-space cube with a perfectly matched layer of 10 cells, voxel edge of 1 mm in the body and graded 1–4 mm outside, and 12 plane-wave directions per frequency at two orthogonal polarizations. Path-level data come from a differentiable ray-tracer [24] with no roughness model. All scripts and input geometries that produced the figures in this section are in the companion code release.

B. Mie theory on lossy spheres

For a lossy sphere of radius a and complex refractive index $\tilde{n}$, the Mie series gives an exact solution for the absorption efficiency Q_{abs}. The geometric law predicts $P_{\mathrm{abs}} = \mathrm{IPD}\, T_0\, \pi a^2$, so its error is $(T_0/Q_{\mathrm{abs}} - 1)$. We use skin properties from the IT'IS database [18], [19] at each frequency. The total error splits into two contributions. The Fresnel approximation error is shape- and frequency-dependent but size-independent. On a sphere it is the sphere ratio $R = T_0/\langle T_{\mathrm{avg}} \rangle$, which crosses unity at approximately 39 GHz (Fig. 4). The diffraction error is size-dependent and scales as $x^{-2/3}$ in the optical regime, where $x = \pi d/\lambda$ is the size parameter. Diffraction bends waves into the geometric shadow, adding absorption that the surface law misses. We refer to the regime where x is small enough that this diffracted contribution exceeds a few percent of total absorption as the *body-Mie regime*. For body-scale targets it corresponds to frequencies below approximately 6 GHz.

Figure 6 shows the Mie validation. Figure 6(a) shows the error versus size parameter at 28 GHz. It converges from below towards the Fresnel limit $R_{\mathrm{sphere}} - 1 \approx -1.2\%$ as $x \to \infty$. Figure 6(b) shows the error versus frequency for four representative body-part diameters.

For body-relevant sizes (head, torso) over 6–100 GHz, the error ranges from 0.4% on a torso at 100 GHz to 14% on a head at 28 GHz, set mostly by diffraction into the geometric shadow at the low end of the band. At 28 GHz the law underestimates absorption. For fingers below 6 GHz, errors exceed 30%. On body-scale objects in the claimed regime, the residual stays within the dielectric uncertainty on T_0 (Fig. 9). Per-frequency residuals across four body-part diameters (17, 80, 180, 300 mm) are in Table **??** of the SI.

C. Full Fresnel on the Thelonious phantom

The Mie test bounds the Fresnel error on a smooth shape. This section validates the theory on a realistic human body. We compare the simplified prediction

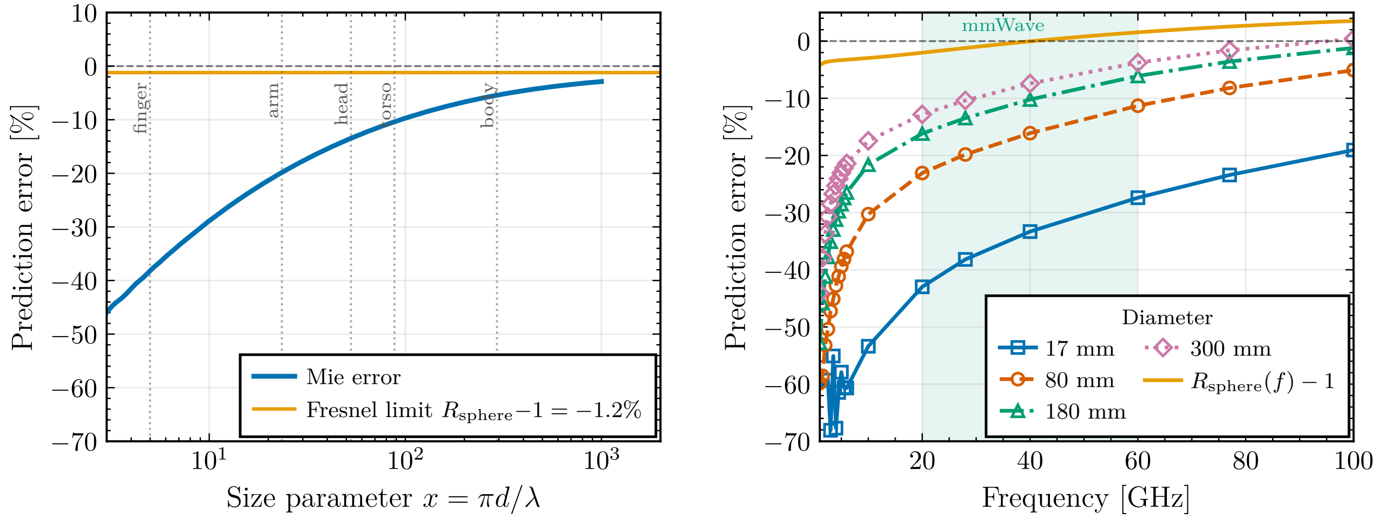

(a) Across size parameter at 28 GHz.

(b) Across frequency for four body-part diameters.

Fig. 6: Mie validation against lossy spheres with frequency-dependent IT'IS skin properties [18], [19]. (a) Prediction error versus size parameter at 28 GHz. Vertical dashed lines mark body-part sizes. The curve converges from below to the Fresnel limit $R_{\text{sphere}} - 1 \approx -1.2\%$ as $x \to \infty$. (b) Prediction error versus frequency for finger (17 mm), arm (80 mm), head (180 mm), and torso (300 mm) diameters. The wireless mmWave band is shaded green. The orange asymptote is $R_{\text{sphere}}(f) - 1$, the size-independent Fresnel limit.

TABLE IV: Geometric law versus full Fresnel integration on the Thelonious phantom (skin at 28 GHz, plane wave from above).

Metric	Simplified	Full Fresnel	Error
Mean APD (illum.)	0.185 W/m^2	0.186 W/m^2	0.5%
Peak APD	0.539 W/m^2	0.539 W/m^2	0.0%

$\text{APD}^{\text{simp}} = \text{IPD}\, T_0\, [\mu]_+$ against the full polarization-aware Fresnel integration $\text{APD}^{\text{full}} = \text{IPD}\, T_{\text{eff}}(\theta, \text{pol})\, [\mu]_+$ on the Thelonious mesh (23 826 triangles, 0.787 m^2 surface area). The incident plane wave comes from above, with skin properties at 28 GHz.

Table IV reports the pointwise comparison. For the 4 907 illuminated triangles with $\theta < 75°$, the local statistics are mean error -2.6%, root-mean-square 3.2%, and range $[-5.3\%, 0.0\%]$. The peak APD is recovered exactly because the maximum is at normal incidence, where $T_{\text{eff}}(0) = T_0$ regardless of polarization. The local error is below 5.5% everywhere with $\theta < 75°$. Section **??** of the SI extends the analysis to 128 illumination directions and three polarization states. The per-direction distribution of total absorbed power clusters around $T_0\, A_\perp$ within the directional spread set by self-shadowing.

D. Sim4Life FDTD on the Thelonious phantom

The Mie and Fresnel tests check approximations against analytic and semi-analytic ground truths. Full Sim4Life FDTD on the same Thelonious mesh, matched dielectric properties, and matched plane-wave excitation completes the comparison. Two regulatory metrics are evaluated. The first is the IEC/IEEE 63195 peak APD averaged over a 4 cm^2 patch. At 7 GHz on three lateral and frontal incidence directions with θ-polarization, the direction-averaged ratio of law to FDTD is 1.027. A $\pm 20\%$ uncertainty on the IT'IS dielectric properties [18], [19] propagates through the Fresnel coefficient at 7 GHz to $\pm 7\%$ on T_0. The direction-averaged ratio falls inside this band. The per-direction values are 1.06, 1.20, and 0.83. The spread beyond $\pm 7\%$ comes from FDTD discretization and per-direction polarization detail in the reference, not the closed form.

The second metric is the direction-averaged Cauchy formula (13) across 12 directions and 2 polarizations at 5.8 GHz. The ratio of law to FDTD on direction-averaged total absorbed power is 1.012, with $A_{\text{ab}}/A = 0.865$ and $\bar{T}(f)$ from Table III. Figure 7 extends the comparison across 0.45–5.8 GHz.

The closed-form Cauchy prediction approaches unity at the upper end of the band. Below 6 GHz the surface law underestimates because body-scale Mie and resonance effects do not enter a surface-only law, in line with the Mie analysis on a sphere of comparable size parameter.

E. Combined dosimetry literature

The literature comparison maps each reported empirical scalar to the corresponding closed-form quantity. Kodera's transmission coefficient T_{tr} is compared with the Fresnel transmission used in the one-dimensional reference model. Flintoft's self-shadowing factor γ_s is compared with the surface mean of the exposure fraction $\eta(\mathbf{r})$. Bamba's efficiency $\eta(f)$ and Zhang's coefficient ξ are compared with the whole-body factor $\bar{T}(f)A_{\text{ab}}/A$. The plotted Flintoft points are linear-regression intercepts of $\langle Q^a \rangle$ at $d_{\text{SF}} = 0$ with $\gamma_s = 1$ [7, Eq. 6]. The plotted Zhang points combine

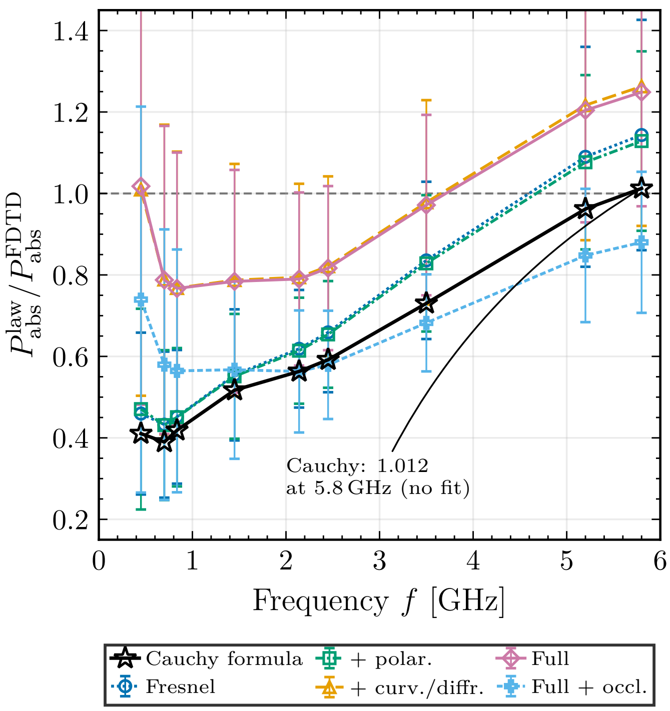

Fig. 7: Closed-form prediction versus Sim4Life FDTD on the Thelonious phantom. Twelve directions and two polarizations per frequency from 0.45–5.8 GHz; error bars show the spread across directions. The kernel curves switch on the corrections of Section V-F in sequence: "Fresnel only" uses T_s/T_p at the convex limit, "+ polarization" adds the polarization-aware T_{eff}, "+ curvature & diffraction" adds the $1/(kR)$ refinement, "Full kernel" is the constant-T_0 geometric law without occlusion, "Full + occlusion" multiplies by $V(\mathbf{r}, \hat{\boldsymbol{k}})$. The Cauchy stars are the closed-form whole-body identity, giving 1.012 at 5.8 GHz. The layered T_{lay} of Section IV-C recovers the sub-6 GHz dip qualitatively.

the 6–18 GHz plateau from [8, Fig. 4.9] with the 1–6 GHz envelope from [8, Fig. 4.11]. Figure 8 then compares the closed-form prediction (13) against 168 volunteers and 5 FDTD phantoms from 1 to 100 GHz.

Table V lists the numerical comparisons. Bamba *et al.* [6]'s η in panel (c) is fit from full-body FDTD on ellipsoidal phantoms in diffuse-field exposure. Their fit absorbs creeping-wave and finite-curvature contributions that the planar-tissue $\bar{T}$ omits. Its convergence to $\bar{T}$ at 5.8 GHz, the upper edge of their calibration range, is the convergence to the geometric-optics regime predicted by a Mie analysis of body-scale spheres [27]. The 1.45–3 GHz portion of their fit lies outside the geometric-optics validity window of the present framework (Table VIII). The systematic divergence in panel (c) below 3 GHz is the body-Mie regime, not a model failure. Bamba *et al.*'s anatomical-phantom validation at 3 GHz returns residuals of −39.4%, −11.7%, +10.7%, and +10.6% on the Thelonious, Billie, Ella, and Duke phantoms [6, Table 7]. The largest divergence is on the smallest phantom. The same mechanism appears in panel (d) on the Diao *et al.* [3] TARO sweep (frontal plane wave, vertical polarization, projected area 0.54 m^2), where T_{eff} rises from 0.43 at 10 GHz to 0.88 at 1 GHz.

Kodera *et al.* [2] report the closest numerical counterpart to the present analysis. Their Fig. 13 compiles whole-body absorbed SAR data over 1–10 GHz at IPD = 10 W/m^2 across nine prior numerical phantom studies and two reverberation-chamber measurement campaigns; their Fig. 6 extends the same comparison to 1–100 GHz on five parametric layered models (Models I–V). The compilation shows the asymptotic plateau that (13) predicts. Kodera *et al.* fit a study-specific T_{tr} per phantom and frequency from a one-dimensional multilayer slab calculation; their homogeneous-skin curve (Fig. 9, right axis) reproduces the Fresnel T_0 within 1–2% above 6 GHz, and oscillates around that value below 6 GHz with a multilayer Fabry–Pérot pattern of the same form as the layered transmission T_{lay} in Section IV-C. Equation (13) supplies the closed-form $T_{\mathrm{tr}} \to \bar{T}(f)$ that all phantoms converge to in the geometric-optics regime. The residual phantom-to-phantom spread is set by the body-shape factor A_{ab}/A.

F. Higher-order corrections

The correction box in the flowchart collects the effects left out by the geometric law. We treat them in turn: curvature, diffraction at the shadow boundary, and inter-body reflections. The kernel labels in Fig. 7 ("Fresnel only," "+ polarization," "+ curvature & diffraction," "Full kernel," "+ occlusion") switch each correction on against the same FDTD reference.

First, we examine the influence of curvature. For a surface with twice the local mean curvature $H = 1/R_1 + 1/R_2$, the first-order Physical Optics correction multiplies the geometric law by $1 + \mu/(kR_1) + \mu/(kR_2)$, where $k = 2\pi/\lambda$ is the free-space wavenumber. Since $[\mu]_+ \cdot \mu = [\mu]_+^2$, the per-triangle update separates additively,

$$\mathrm{APD}^{(j)} = T_0 \sum_i S_i \left[[\mu_{ji}]_+ + \frac{H_j}{k} \, [\mu_{ji}]_+^2 \right] V_{ji} \, , \qquad (15)$$

adding a quadratic gate on top of the linear one. The magnitude is set by $1/(kR)$. Table VI lists the correction at 28 GHz on representative body parts.

The correction grows as the wavelength approaches the local body-part size. At sub-6 GHz frequencies the smallest features have $kR \lesssim 5$ where the correction is no longer small. At 28 GHz, only the ear edges and fingertips carry a correction above the Fresnel error floor.

Second, we quantify the effect of diffraction at the shadow boundary. The sharp $[\cdot]_+$ cutoff at $\mu = 0$ is a geometric-optics idealization. Diffraction smooths the shadow edge over a Fresnel-zone width $\sqrt{\lambda R_j}$. The physical activation becomes

$$\mu \mapsto \mu \, \tfrac{1}{2} [1 + \mathrm{erf}(\mu/\sigma_j)] \, , \qquad \sigma_j = \sqrt{\lambda/(2\pi R_j)} \, . \qquad (16)$$

The ICNIRP centimeter-scale spatial averaging regularizes the boundary at a length scale larger than σ_j across the

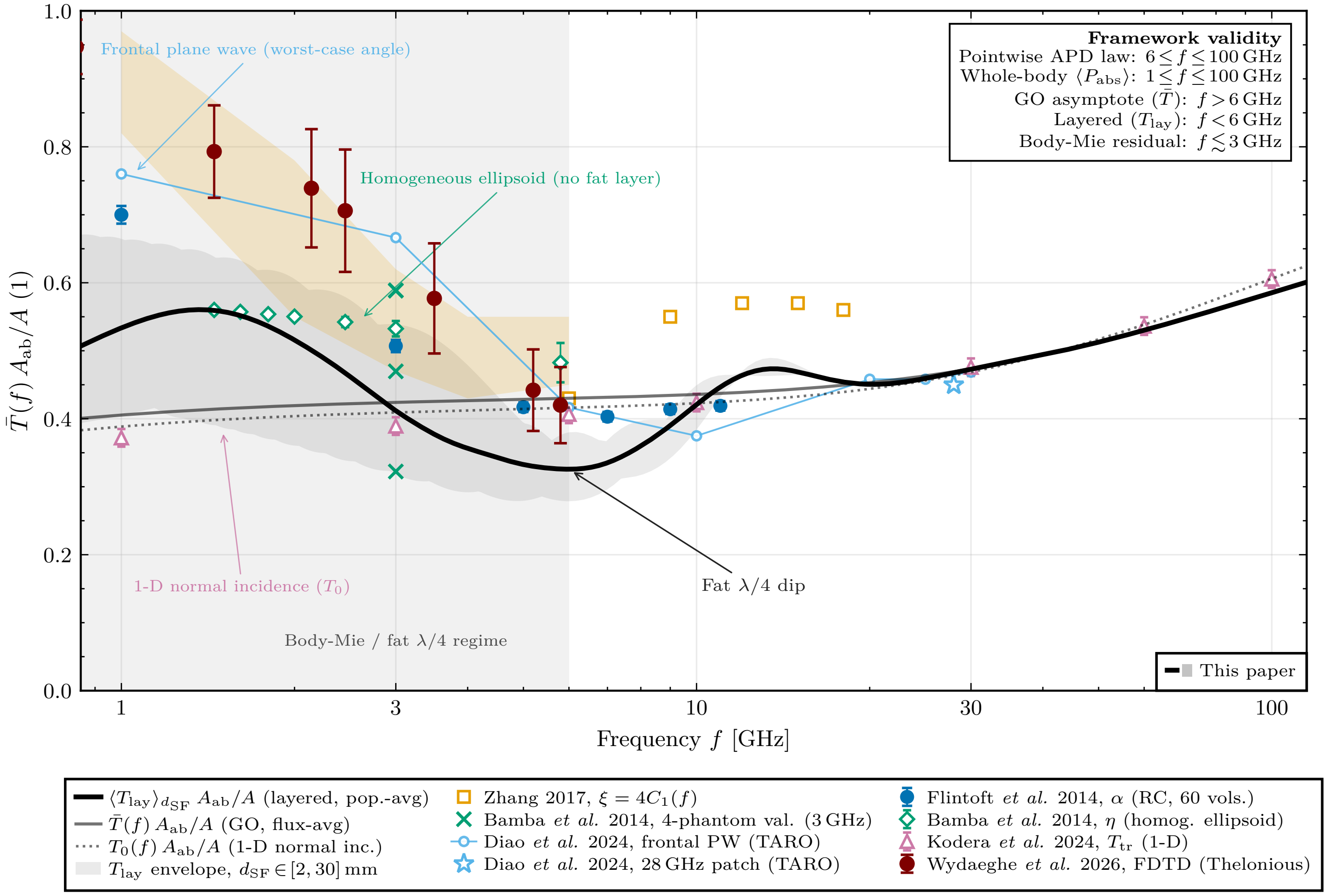

Fig. 8: Closed-form prediction (13) compared with direction-averaged whole-body absorption ratios from the dosimetry literature. The thick black line uses the population-averaged layered transmission, the thin black line is the geometric-optics asymptote $\bar{T}(f)A_{\mathrm{ab}}/A$, and the dotted line is the normal-incidence reference $T_0(f)A_{\mathrm{ab}}/A$. The gray band shows the layered-transmission envelope for subcutaneous-fat thicknesses $d_{\mathrm{SF}} \in [2, 30]$ mm. Error bars are standard errors of the mean. The inset gives framework validity by frequency band.

TABLE V: Quantitative comparison of the closed-form prediction to the empirical literature. The shaded sub-3 GHz regime, where the layered tissue model in Section IV-C replaces $\bar{T}$, is excluded.

Reference	Empirical observation	Closed-form prediction	Match
Flintoft [7]	$\langle Q^a \rangle/\gamma_s = 0.47$–$0.49$ at 7–11 GHz, 60 volunteers	$T_0(f) = 0.48$ at 9 GHz, $\bar{T}(f) = 0.50$	2%–4%
Bamba [6]	$\eta(f) = 0.48$–0.56 at 1.45–5.8 GHz, four FDTD ellipsoids	$\bar{T}(f) = 0.47$–0.50	3% at 5.8 GHz; convergent with frequency
Zhang [8]	$\xi = 0.45$–0.65 at 6–18 GHz, 48 subjects	$\bar{T}(f) \cdot A_{\mathrm{ab}}/A = 0.43$–$0.49$	within scatter
Kodera [2]	T_{tr} matches $A_{\perp}$ scaling at 10–100 GHz, parametric FDTD	$T_{\mathrm{tr}} \equiv T_0$	$\leq 5\%$
Diao [3]	$T = 0.52$ at 28 GHz, anatomical FDTD	$T_0 = 0.536$ at 28 GHz	3%
Flintoft [7]	$-0.0061\,\mathrm{mm}^{-1}$ slope of $\langle Q^a \rangle$ vs d_{SF} at 3 GHz	Layered Fabry–Pérot in fat	mechanism, qualitative

wireless band, so the diffraction correction is significant only for high-resolution local maps or for comparisons against point measurements. The integrated effect on whole-body absorbed power on the Thelonious phantom is 1.2% at 28 GHz, below 1% above 30 GHz, and several percent below 6 GHz, in line with the Mie analysis on body-scale spheres in Section V-B. Numerical values across 1–100 GHz on the Thelonious phantom are in Table **??** of the SI.

Finally, we study the impact of inter-body reflections. At a surface point the fraction T_0 is absorbed and the remaining $1 - T_0 \approx 0.46$ is reflected. On a nonconvex body, part of this reflected power re-illuminates another point and contributes to absorption that the first-bounce law omits. The radiosity series gives a multiplier $C(\mathbf{r}) = 1/(1 - \bar{R}\, f(\mathbf{r}))$ at each point, where $\bar{R} = 1 - \bar{T} \approx 0.46$ is the flux-weighted reflectance and $f(\mathbf{r}) \leq 1 - \eta(\mathbf{r})$ is the recapture fraction bounded by the local nonvisible hemisphere area.

Two effects keep the body-averaged correction small.

TABLE VI: Curvature correction at 28 GHz ($k \approx 587\ \mathrm{m}^{-1}$). The correction is below the Fresnel approximation error for most body regions and concentrates at small features.

Region	R [mm]	$1/(kR)$	Correction
Torso, head	> 100	$< 0.2\%$	negligible
Arm	approx. 40	0.4%	approx. 0.4%
Finger	approx. 8	2.1%	approx. 2%
Ear edge	approx. 2	8.5%	approx. 8%

First, the bound $f \leq 1 - \eta$ self-compensates: deep concavities (η low) have a high recapture fraction (f high), so the product $\eta{\cdot}C$ varies much less than η alone. Second, specular reflection at mmWave (skin meets the Rayleigh roughness criterion) reduces f by roughly a factor of three relative to the diffuse bound. On the Thelonious phantom at 28 GHz, the area-weighted recapture fraction is $f_{\mathrm{global}} \approx 0.09$ under the diffuse bound, giving $C \approx 1.04$. The specular estimate brings this to $C \approx 1.01$. The body-averaged correction stays below 2%, smaller than the propagated dielectric uncertainty derived in Section V-G. The convex-hull energy bound $\langle P_{\mathrm{abs}} \rangle \leq \mathrm{IPD}\, A_{\mathrm{CH}}/4$ brackets the true absorbed power within $A_{\mathrm{CH}}/A \approx 1.20$ on Thelonious.

G. Error budget

Figure 9 reports two regimes side by side at 28 GHz on skin. The worst case is single body part, single direction, pointwise local. The typical case is whole-body integrated, direction-averaged. The dielectric input spread is $\pm 20\%$ on ε_r and σ. This is the inter-model gap between Gabriel *et al.* [19] and the empirical Gabriel-times-1.2 fit that Christ *et al.* [28] obtained from S_{11} measurements on 37 volunteers at 40–110 GHz. The spread is consistent with mmWave dielectric campaigns more broadly [22], [29], [30]. We evaluate $T_0 = 4n/[(1+n)^2 + \kappa^2]$ at the four corners of the $\pm 20\%$ box. The largest deviation on skin at 28 GHz is $\pm 7\%$. The Fresnel approximation worst case is 5.3% pointwise local (Table IV). The typical case is 1.2% direction-averaged on whole-body absorbed power (Supplementary Information, 128-direction sweep). The diffraction worst case is 10% on a torso-scale Mie sphere (Section V-B). The typical case is 1.2% integrated on Thelonious (Supplementary Information, GELU integration). The inter-body reflection worst case is 4% under the diffuse bound. The typical case is 1% under specular at mmWave (Section V-F). In the typical case every model error stays below the dielectric uncertainty.

VI. Compliance bounds

Proven bounds on the ICNIRP basic restrictions follow in closed form from the incident power density. Section VI-A bounds the incident power density allowed for whole-body SAR. Section VI-B bounds the peak spatial-average SAR over a 10 g cube.

A. Whole-body SAR threshold

The ICNIRP 2020 guidelines [1] specify a whole-body average SAR limit of 0.08 W/kg for the general public.

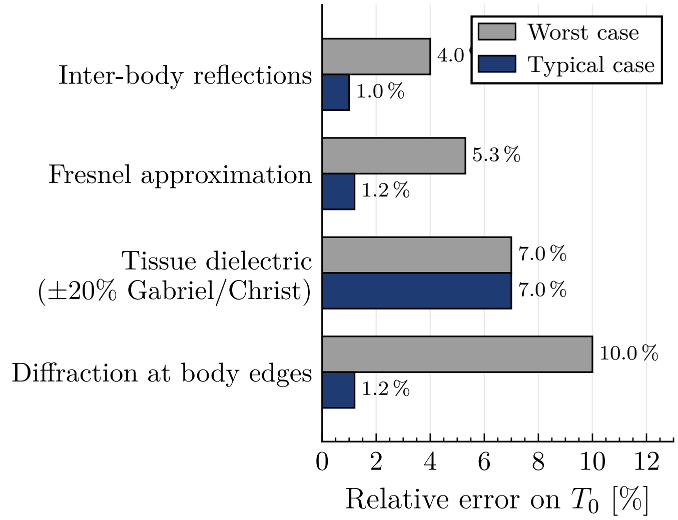

Fig. 9: Error budget for the geometric law in two regimes at 28 GHz on skin. Worst case is single body part, single direction, pointwise. Typical case is whole-body integrated, direction-averaged. Only the dielectric uncertainty stays large in the typical case.

TABLE VII: Worst-case compliance threshold across the human population at 28 GHz with $\bar{T} = 0.543$. The threshold varies by a factor of about two between an infant and a large adult.

Body type	m [kg]	h [cm]	$\mathrm{IPD}_{\max}$ [W/m^2]
Infant (1 yr)	8	70	6.2
Child (6 yr)	20	110	7.6
Adolescent	50	160	9.9
Adult (ref.)	70	170	11.4
Large adult	100	180	13.5

The bound $A_\perp(\hat{\boldsymbol{k}}) \leq A/2$ on closed surfaces gives $D(\hat{\boldsymbol{k}}) \leq 2A/A_{\mathrm{ab}}$. With $\mathrm{SAR}_{\mathrm{wb}} = P_{\mathrm{abs}}/m$ and the conservative replacement $A_{\mathrm{ab}} \leq A$, the worst-case threshold is

$$\mathrm{IPD}_{\max} = \frac{0.16\, m}{\bar{T}\, A}\,, \tag{17}$$

a closed-form function of body mass m, body surface area A, and tissue transmission $\bar{T}$, none of which requires an FDTD solve on the specific exposure scenario.

Body surface area follows the Du Bois formula [31] $A \approx 0.007184\, m^{0.425}\, h^{0.725}$ with mass in kg and height in cm, so $\mathrm{IPD}_{\max}$ scales as $m/A \propto \mathrm{BMI}^{0.575}\, h^{0.425}$. Table VII evaluates (17) on a representative population at 28 GHz with $\bar{T} = 0.543$. The scaling matches the observation in the dosimetry literature [32], [33] that absorption cross-section scales with surface area while mass scales with volume. Section **??** of the SI derives the Du Bois scaling and bounds the linearly polarized worst-case correction to (17) via the body polarization directivity.

Implications for the existing ICNIRP general-public reference level above 6 GHz are stated in Section VII-B.

B. Peak spatial-average SAR over a 10 g cube

Below 6 GHz the ICNIRP basic restriction is the peak spatial-average SAR over a 10 g cube [1], [34]. An energy-conservation argument on the cube footprint bounds this restriction by the absorbed power density, so no explicit cube search is needed.

The following bound links the cube quantity to APD.

Theorem 2. *For an axis-aligned* 10 *g cube placed per IEC/IEEE 62704-1 on a planar three-layer body, the peak spatial-average SAR satisfies*

$$\mathrm{psSAR}_{10\mathrm{g}} \;\le\; \frac{\sqrt{2}\,\langle \mathrm{APD}\rangle_{1\,/\,4\,\mathrm{cm}^2}}{\rho_m\, L}\,, \tag{18}$$

where $L = (m/\rho_m)^{1/3} = 21.5$ *mm and* $\langle \mathrm{APD}\rangle_{1\,/\,4\,\mathrm{cm}^2}$ *is the local absorbed power density. At the ICNIRP basic restriction* $\langle \mathrm{APD}\rangle_{1\,/\,4\,\mathrm{cm}^2} \le 10$ *W/m*^{2}*, this implies* $\mathrm{psSAR}_{10\mathrm{g}} \le 0.66$ *W/kg, a factor of three below the head and trunk basic restriction of* 2 *W/kg and a factor of six below the limb restriction of* 4 *W/kg.*

The bound follows from energy conservation on the cube footprint, with the $\sqrt{2}$ factor covering the worst-case tilt between cube axes and body normal. Section **??** of the SI derives the bound, gives the cube-intersection geometry under the IEC mass rule, and confirms it on Thelonious to within a median ratio of 1.30. The same surface integral that delivers $\langle \mathrm{APD}\rangle_{1\,/\,4\,\mathrm{cm}^2}$ therefore controls $\mathrm{psSAR}_{10\mathrm{g}}$.

VII. Discussion

A. Computational structure

The matrix form (10) is a single-hidden-layer rectified-linear 'network' whose weights are the path directions and powers from a ray tracer [24]. Three properties follow.

First, the network is differentiable in every input. Replacing the hard $[\cdot]_+$ gate with the smooth GELU activation (16) preserves the chain rule. Gradients of regulatory quantities propagate to antenna positions, antenna orientations, beam codebooks, and reconfigurable-intelligent-surface phases through standard backpropagation. End-to-end exposure assessment in current practice carries a per-scenario FDTD evaluation on the user phantom as the back-end step [35], [36]. With the closed form replacing that step, exposure-constrained network design becomes a continuous optimization problem.

Second, the per-triangle absorbed-power map for $M \approx 10^4$ triangles and $N \approx 10^2$ paths is one matrix-vector multiply on a modern GPU, evaluated in under 10 ms. The cost is independent of frequency. Against an FDTD reference whose cost scales as f^4, the speed advantage grows by roughly 10^4 from 6 to 60 GHz, exactly the band where the Fresnel approximation is sharpest and the closed form holds pointwise within 3% of FDTD (Table VIII). The cosine gate is rectified shading. The visibility matrix $\mathbf{V}$ is ambient occlusion, one of the most optimized computations in real-time rendering [14].

Third, the whole-body identity (13) factorizes the body dependence into a single scalar $A_{\mathrm{ab}} = \bar{\eta}\, A$. For a given phantom and posture, $\bar{\eta}$ is computed once, in tens of milliseconds, and cached. Population studies that previously required one FDTD solve per body and per direction reduce to one Fresnel quadrature shared across the population and one occlusion pass per body.

B. Regulatory implications

Whole-body ICNIRP compliance reduces to one inequality on three precomputed scalars (Eq. (17)). The same algebra evaluates the existing reference levels for under- or over-protection across the population without an FDTD campaign.

The ICNIRP general-public reference level above 6 GHz is 10 W/m^2 [1]. Reference levels are the operationally measured incident-power-density limits intended to imply compliance with the underlying basic restriction, here 0.08 W/kg whole-body SAR. Setting $\mathrm{IPD}_{\max} = 10$ W/m^2 in (17) returns the threshold $m/A \ge 33.9$ kg/m^2 at $\bar{T} = 0.543$ (28 GHz on skin). Table VII lists $\mathrm{IPD}_{\max}$ values of 6.2, 7.6, and 9.9 W/m^2 for the infant, the six-year-old child, and the adolescent under the worst-case directional bound $D \le 2A_{\mathrm{CH}}/A_{\mathrm{ab}}$. The reference level exceeds these thresholds by 61%, 32%, and 1% respectively.

The closed form gives a closed-form certificate that the existing reference level fails the basic restriction for the three smaller body sizes under worst-case directional exposure. Under realistic plane-wave or multipath exposure the directivity is below this worst case, and the basic restriction is met [1]. The closed form makes both the worst-case and the directional-average evaluation explicit.

C. Regime of validity

Table VIII summarizes the resulting band stratification.

Equations (9) and (13) hold quantitatively above approximately 1 GHz on whole-body absorbed power and above approximately 6 GHz pointwise on the surface, with documented sub-6 GHz behavior from (14). The low-frequency boundary is set by three independent physical scales: body opacity, the body-scale Mie regime, and whole-body resonance. The high-frequency boundary is set by two, the softening of the pseudo-Brewster compensation and skin surface roughness, both gentler than the low-frequency boundary.

The surface law requires the body to be optically thick to the incident wave: the tissue skin depth must stay smaller than the body characteristic dimension, otherwise the wave passes through rather than being absorbed at the surface. This opacity criterion places the lower validity limit near 700 MHz–1 GHz for limbs and near 250 MHz for a torso. The tissue-property database [19] gives muscle skin-depth values that exceed limb cross-sections below approximately 1 GHz and torso cross-sections below approximately 250 MHz.

The Mie regime sets a second lower limit. The geometric-optics asymptote holds with sub-percent residual once $ka \gtrsim 30$ on a body characteristic dimension, and Section V-B quantifies the residual on body-scale spheres.

TABLE VIII: Frequency-band limits of (13) on a human-adult body. Quantitative validity covers 1–100 GHz on whole-body absorbed power, 6–100 GHz pointwise on the surface.

Band	Surface law status	Whole-body identity
below 300 MHz	other physics: resonance and hot-spots	FDTD required
0.3–1 GHz	qualitative, 10%–30% Mie underestimate	qualitative, T_{lay} recovers the dip
1–6 GHz	integrated within 5%–10%, local map loses pointwise meaning	quantitative, T_{lay} replaces T_0
6–100 GHz	quantitative within 3% pointwise	quantitative, Brewster compensation sharpest

Whole-body resonance dominates below approximately 300 MHz, where the body acts as a half-wave dipole and surface absorbed power is unrelated to internal hot-spots [37]. Below this frequency the framework reduces to volumetric solvers.

The pseudo-Brewster compensation softens above 200–250 GHz, where the Azzam high-index criterion $|\tilde{n}| > 2.5$ weakens and worst-case angular variation grows from 5.6% at 28 GHz to approximately 10% at 250 GHz and 15% at 300 GHz, comparable to the dielectric uncertainty on T_0 (Fig. 9). Skin refractive-index modulus from the IT'IS database [18], [19] is 4.84 at 28 GHz, 3.68 at 60 GHz, and 3.01 at 100 GHz, and extrapolation puts $|\tilde{n}|$ near 2.5 around 200–250 GHz, approximately 2.2 at 300 GHz, and 1.8–2 at 1 THz.

Skin roughness sets an upper limit near 1 THz, where the Rayleigh criterion $h \cos\theta/\lambda < 1/8$ is violated on papillary-ridge-scale features and diffuse scattering becomes the dominant correction. Skin features are stratified into stratum-corneum microtexture at 10–100 μm, papillary ridges at 0.4–0.5 mm spacing, and gross body curvature at centimeters. Wavelength is 3 mm at 100 GHz, 1 mm at 300 GHz, 0.3 mm at 1 THz. The Rayleigh criterion is met at 100 GHz on ridge-scale features and is marginal at 300 GHz.

For sources in the reactive near field ($d < \lambda/(2\pi)$, that is 1.7 mm at 28 GHz), evanescent waves and antenna-body impedance coupling require full-wave simulation. Outside this regime, the law applies pointwise with spatially varying inputs.

The dielectric properties of biological tissue have been measured to within approximately 20% at mmWave [22]. This input uncertainty produces ±7% on T_0 through the sublinear propagation derived in Section V-G, and it dominates the error budget at every operating regime where the surface law applies.

VIII. Conclusion

A closed-form method is proposed for the absorbed power density on biological tissue from 1 to 100 GHz. The whole-body absorbed power factors into a flux-weighted Fresnel transmission $\bar{T}(f)$ times a body shape factor A_{ab}/A.

The cost decouples from frequency. The f^4 FDTD scaling collapses to one matrix-vector multiply with positive-part gating, differentiable in antenna position, orientation, beam codebooks, and reconfigurable-intelligent-surface phases. A simulation campaign that takes weeks of FDTD reduces to a tissue-property lookup and an ambient-occlusion pass on the body mesh.

Two extensions follow naturally. Coherent beamforming replaces summed powers with summed amplitudes on short-range mmWave devices. At mmWave the far-field distance shrinks to centimeters, so the device antenna pattern maps directly onto the body surface (Section VII-C). Pre-compliance for handheld uplink follows in closed form.

References

[1] International Commission on Non-Ionizing Radiation Protection, "Guidelines for limiting exposure to electromagnetic fields (100 kHz to 300 GHz)," *Health Phys.*, vol. 118, no. 5, pp. 483–524, May 2020, doi: 10.1097/HP.0000000000001210.

[2] S. Kodera, K. Taguchi, Y. Diao, T. Kashiwa, and A. Hirata, "Computation of whole-body average SAR in realistic human models from 1 to 100 GHz," *IEEE Trans. Microw. Theory Techn.*, vol. 72, no. 1, pp. 91–100, Jan. 2024, doi: 10.1109/TMTT.2023.3289562.

[3] Y. Diao, S. Kodera, K. Li, and A. Hirata, "Assessment of whole-body-average SAR for exposure to electromagnetic fields up to 30 GHz using a body model with scaled dielectric parameters," *IEEE Trans. Electromagn. Compat.*, vol. 66, no. 5, pp. 1351–1360, Oct. 2024, doi: 10.1109/TEMC.2024.3421521.

[4] A. Hirata, S. Kodera, K. Sasaki, J. Gomez-Tames, I. Laakso, A. Wood, S. Watanabe, and K. R. Foster, "Human exposure to radiofrequency energy above 6 GHz: review of computational dosimetry studies," *Phys. Med. Biol.*, vol. 66, no. 8, Apr. 2021, Art. no. 08TR01, doi: 10.1088/1361-6560/abf1b7.

[5] R. Wydaeghe, B. Stroobandt, S. Gallucci, M. Parazzini, G. Tognola, J. Wiart, G. Vermeeren, M. Guxens, E. Tanghe, and W. Joseph, "Environmental and auto-induced RF-EMF adult and children far-field exposure simulations between 450 MHz and 26 GHz," *Phys. Med. Biol.*, 2026, under review.

[6] A. Bamba, W. Joseph, G. Vermeeren, A. Thielens, E. Tanghe, and L. Martens, "A formula for human average whole-body $\mathrm{SAR}_{\mathrm{wb}}$ under diffuse fields exposure in the GHz region," *Phys. Med. Biol.*, vol. 59, no. 23, pp. 7435–7456, Dec. 2014, doi: 10.1088/0031-9155/59/23/7435.

[7] I. D. Flintoft, M. P. Robinson, G. C. R. Melia, A. C. Marvin, and J. F. Dawson, "Average absorption cross-section of the human body measured at 1–12 GHz in a reverberant chamber: Results of a human volunteer study," *Phys. Med. Biol.*, vol. 59, no. 13, pp. 3297–3317, Jul. 2014, doi: 10.1088/0031-9155/59/13/3297.

[8] X. Zhang, "Accurate wideband measurement of human body absorption cross section in a reverberation chamber: A morphological parameters study from 1 GHz to 18 GHz," Ph.D. dissertation, Dept. Electron., Univ. York, York, U.K., 2017. [Online]. Available: https://etheses.whiterose.ac.uk/19455/

[9] X. Zhang, M. P. Robinson, I. D. Flintoft, J. F. Dawson, and S. Parker, "Morphological study on human body absorption cross section in a reverberation chamber from 1 GHz to 16 GHz," *IEEE Trans. Electromagn. Compat.*, vol. 62, no. 2, pp. 330–337, Apr. 2020.

[10] R. M. A. Azzam, "High-index dielectric substrates with nearly constant reflectance for incident unpolarized or circularly polarized light over a wide range of incidence angles," *J. Mod. Opt.*, vol. 62, no. 10, pp. 811–815, Jun. 2015.

[11] A.-L. Cauchy, "Mémoire sur la rectification des courbes et la quadrature des surfaces courbes," *C. R. Acad. Sci. Paris*, vol. 13, pp. 1129–1146, 1841.

[12] S. Zhukov, A. Iones, and G. Kronin, “An ambient light illumination model,” in *Rendering Techniques ’98 (Proc. 9th Eurographics Workshop Rendering)*, G. Drettakis and N. Max, Eds. Vienna, Austria: Springer, 1998, pp. 45–56.

[13] H. Landis, “Production-ready global illumination,” in *ACM SIGGRAPH 2002 Course Notes*, vol. 16, San Antonio, TX, USA, Jul. 2002, pp. 87–102.

[14] T. Akenine-Möller, E. Haines, and N. Hoffman, *Real-Time Rendering*, 4th ed. Boca Raton, FL, USA: A K Peters/CRC Press, 2018.

[15] M. Born and E. Wolf, *Principles of Optics*, 7th ed. Cambridge, U.K.: Cambridge Univ. Press, 1999.

[16] R. F. Potter, “Pseudo-Brewster angle and the optical constants,” *Appl. Opt.*, vol. 9, no. 7, p. 1717, Jul. 1970.

[17] G. P. Ohman, “The pseudo-Brewster angle,” *IEEE Trans. Antennas Propag.*, vol. 25, no. 6, pp. 903–904, Nov. 1977.

[18] IT’IS Foundation, “Tissue properties database V5.0,” Zürich, Switzerland, 2024. [Online]. Available: https://itis.swiss/virtual-population/tissue-properties/database/

[19] S. Gabriel, R. W. Lau, and C. Gabriel, “The dielectric properties of biological tissues: III. Parametric models for the dielectric spectrum of tissues,” *Phys. Med. Biol.*, vol. 41, no. 11, pp. 2271–2293, Nov. 1996, doi: 10.1088/0031-9155/41/11/003.

[20] T. Samaras and N. Kuster, “Theoretical evaluation of the power transmitted to the body as a function of angle of incidence and polarization at frequencies >6 GHz and its relevance for standardization,” *Bioelectromagnetics*, vol. 40, no. 2, pp. 136–139, Feb. 2019.

[21] D. Funahashi, A. Hirata, S. Kodera, and K. R. Foster, “Area-averaged transmitted power density at skin surface as metric to estimate surface temperature elevation,” *IEEE Access*, vol. 6, pp. 77 665–77 674, 2018, doi: 10.1109/ACCESS.2018.2883733.

[22] S. I. Alekseev and M. C. Ziskin, “Human skin permittivity determined by millimeter wave reflection measurements,” *Bioelectromagnetics*, vol. 28, no. 5, pp. 331–339, Jul. 2007, doi: 10.1002/bem.20308.

[23] D. Hendrycks and K. Gimpel, “Gaussian error linear units (GELUs),” Jun. 2016. [Online]. Available: https://arxiv.org/abs/1606.08415

[24] J. Hoydis, F. Aït Aoudia, S. Cammerer, M. Nimier-David, N. Binder, G. Marcus, and A. Keller, “Sionna RT: Differentiable ray tracing for radio propagation modeling,” Mar. 2023. [Online]. Available: https://arxiv.org/abs/2303.11103

[25] H. Tomita, T. Tagawa, and T. Wagai, “Comparison of formulae for measuring body surface area in Japanese subjects,” *J. Tokyo Med. Univ.*, vol. 57, pp. 519–527, 1999.

[26] W. C. Chew, *Waves and Fields in Inhomogeneous Media.* New York, NY, USA: IEEE Press, 1995.

[27] C. F. Bohren and D. R. Huffman, *Absorption and Scattering of Light by Small Particles.* New York, NY, USA: Wiley, 1983.

[28] A. Christ, A. Aeschbacher, F. Rouholahnejad, T. Samaras, B. Tarigan, and N. Kuster, “Reflection properties of the human skin from 40 to 110 GHz: A confirmation study,” *Bioelectromagnetics*, vol. 42, no. 7, pp. 562–574, Oct. 2021, doi: 10.1002/bem.22362.

[29] K. Sasaki, K. Wake, and S. Watanabe, “Measurement of the dielectric properties of the epidermis and dermis at frequencies from 0.5 GHz to 110 GHz,” *Phys. Med. Biol.*, vol. 59, no. 16, pp. 4739–4747, Aug. 2014, doi: 10.1088/0031-9155/59/16/4739.

[30] M. Zhadobov, N. Chahat, R. Sauleau, C. Le Quement, and Y. Le Drean, “Millimeter-wave interactions with the human body: state of knowledge and recent advances,” *Int. J. Microw. Wirel. Technol.*, vol. 3, no. 2, pp. 237–247, Apr. 2011, doi: 10.1017/S1759078711000122.

[31] D. Du Bois and E. F. Du Bois, “Clinical calorimetry: Tenth paper. A formula to estimate the approximate surface area if height and weight be known,” *Arch. Intern. Med.*, vol. 17, no. 6, pp. 863–871, Jun. 1916, doi: 10.1001/archinte.1916.00080130010002.

[32] A. Hirata, Y. Nagaya, O. Fujiwara, T. Nagaoka, and S. Watanabe, “Correlation between absorption cross section and body surface area of human for far-field exposure at GHz bands,” in *Proc. IEEE Int. Symp. Electromagn. Compat. (EMC)*, Honolulu, HI, USA, Jul. 2007, pp. 1–4.

[33] P. J. Dimbylow, “Fine resolution calculations of SAR in the human body for frequencies up to 3 GHz,” *Phys. Med. Biol.*, vol. 47, no. 16, pp. 2835–2846, Aug. 2002, doi: 10.1088/0031-9155/47/16/301.

[34] *Determining the Peak Spatial-Average Specific Absorption Rate (SAR) in the Human Body From Wireless Communications Devices, 30 MHz to 6 GHz–Part 1: General Requirements for Using the Finite-Difference Time-Domain (FDTD) Method for SAR Calculations*, IEC/IEEE Standard 62704-1-2017, 2017.

[35] R. Wydaeghe, S. Shikhantsov, E. Tanghe, G. Vermeeren, L. Martens, P. Demeester, and W. Joseph, “Realistic human exposure at 3.5 and 28 GHz for distributed and collocated MaMIMO in indoor environments using hybrid ray-tracing and FDTD,” *IEEE Access*, vol. 10, pp. 130 996–131 004, 2022, doi: 10.1109/ACCESS.2022.3227107.

[36] R. Wydaeghe, S. Shikhantsov, G. Vermeeren, L. Martens, E. Tanghe, and W. Joseph, “Hybrid ray-tracing-QuaDRiGa/FDTD method for realistic 28 GHz exposure with 6G CF-MaMIMO in 3D outdoor environments,” *npj Wireless Technol.*, vol. 2, no. 1, art. no. 13, Apr. 2026, doi: 10.1038/s44459-026-00031-4.

[37] C. H. Durney, H. Massoudi, and M. F. Iskander, *Radiofrequency Radiation Dosimetry Handbook*, 4th ed. Brooks Air Force Base, TX, USA: USAFSAM, 1986, USAFSAM-TR-85-73.